Title

High Contrast Ultrasonic Method With Multi-Spatiotemporal Compounding for Monitoring Catheter-Based Ultrasound Thermal Therapy: Development and Ex Vivo Evaluations

Journal

IEEE Transactions on Biomedical Engineering, 68(10)

ISSN

0018-9294

Authors

Wang, Diya
Adams, Matthew S
Jones, Peter D
et al.

Publication Date

2021-10-01

DOI

10.1109/tbme.2021.3067910

Peer reviewed

HHS Public Access

Author manuscript

IEEE Trans Biomed Eng. Author manuscript; available in PMC 2022 October 01.

Published in final edited form as:

IEEE Trans Biomed Eng. 2021 October ; 68(10): 3131–3141. doi:10.1109/TBME.2021.3067910.

High contrast ultrasonic method with multi-spatiotemporal compounding for monitoring catheter-based ultrasound thermal therapy: Development and *Ex Vivo* Evaluations

Diya Wang, **Matthew S. Adams**, **Peter D. Jones**, **Dong Liu**, **Everette C. Burdette**, **Chris J. Diederich***

D. Wang is now with the Key Laboratory of Biomedical Information Engineering of Ministry of Education, School of Life Science and Technology, Xi'an Jiaotong University, Xi'an, China, 710049, and was with the Department of Radiation Oncology, University of California San Francisco, San Francisco, CA, USA, 94115. M. S. Adams, P. Jones, and D. Liu are with the Department of Radiation Oncology, University of California San Francisco, San Francisco, CA, USA, 94115. E. C. Burdette is with the Acoustic Medsystems Inc., Savoy, IL, USA, 61874. C. J. Diederich is with the Department of Radiation Oncology, University of California San Francisco, San Francisco, CA, USA, 94115.

Abstract

Objective: Changes in ultrasound backscatter energy (CBE) imaging can monitor thermal therapy. Catheter-based ultrasound (CBUS) can treat deep tumors with precise spatial control of energy deposition and ablation zones, of which CBE estimation can be limited by low contrast and robustness due to small or inconsistent changes in ultrasound data. This study develops a multi-spatiotemporal compounding CBE (MST-CBE) imaging approach for monitoring specific to CBUS thermal therapy.

Methods: E*x vivo* thermal ablations were performed with stereotactic positioning of a 180° directional CBUS applicator, temperature monitoring probes, endorectal US probe, and subsequent lesion sectioning and measurement. Five frames of raw radiofrequency data were acquired throughout in 15s intervals. Using window-by-window estimation methods, absolute and positive components of MST-CBE images at each point were obtained by the compounding ratio of squared envelope data within an increasing spatial size in each short-time window.

Results: Compared with conventional US, Nakagami, and CBE imaging, the detection contrast and robustness quantified by tissue-modification-ratio improved by 37.2±4.7 (p<0.001), 37.5±5.2 (p<0.001), and 6.4±4.0 dB (p<0.05) in the MST-CBE imaging, respectively. Correlation coefficient and bias between cross-sectional dimensions of the ablation zones measured in tissue sections and estimated from MST-CBE were up to 0.91 (p<0.001) and −0.02 mm^2, respectively.

Conclusion: The MST-CBE approach can monitor the detailed changes within target tissues and effectively characterize the dimensions of the ablation zone during CBUS energy deposition.

*Correspondence: Chris.Diederich@ucsf.edu.

Significance: The MST-CBE approach could be practical for improved accuracy and contrast of monitoring and evaluation for CBUS thermal therapy.

Index Terms—

catheter-based ultrasound; thermal therapy; change in backscatter energy; ultrasound monitoring; tissue-modification-ratio

I. INTRODUCTION

Thermal ablation therapies as delivered by multiple energy modalities can deposit heat to target tissues to induce protein denaturation and coagulation necrosis and have been widely used in such treatments of various solid cancer tumors, abnormal benign tissue, and generalized tissue modification and remodeling [1–5]. As an essential tool, thermal ablation therapies need image guidance for pre-treatment applicator positioning, therapy monitoring and feedback control during ablation, and post-procedure assessment[5–7]. Magnetic resonance imaging (MRI)[8, 9], computerized tomography (CT)[10, 11], and ultrasound (US) imaging[12–15] have been used in monitoring and guiding thermal ablation therapies using extracorporeal or invasive energy modalities including high-intensity focused ultrasound (HIFU)[8, 9], radiofrequency (RF) currents[16], microwaves (MW)[17], and high-intensity catheter-based ultrasound (CBUS)[5, 6, 18]. MRI thermal imaging provides the most accurate imaging modality to monitor in real-time the temperature and thermal dose, and post-procedure verification [8, 9]. Alternatively, CT imaging and corresponding change in Hounsfield units during ablation can also be an indicator to monitor the thermal lesion[10, 11]. Based on changes in backscatter echoes and tissue stiffness during heating, US imaging provides multiple options including conventional B-mode[12–14] and strain imaging[15] for the real-time monitoring of changes in thermal lesion volume. Further, US imaging has the advantages of not relying on ionizing radiation, better portability, and more practical integration within the interventional workflow, with potential for fast real-time feedback of the thermal process and target localization[18].

Numerous US echo-based parametric imaging technologies [15, 19–22] have been developed for the enhancement of detection sensitivity of ablation lesions generated in RF, MW, and HIFU therapies. These technologies also have been used to evaluate the increases in temperature and energy deposition in target tissues during ablation and post-ablation periods. These parameters estimated from US backscatter echoes include echo-time shift[15], attenuation coefficient[21], K parameter[19], Nakagami parameter[20], and backscattered energy[22]. However, these US imaging methods can be limited in specific situations by the low sensitivity in the detection of changes in temperature and thermal tissue related changes during heating.

Considering the requirements of motion and tissue necrosis for echo-time shift based methods[15] and high-temperature elevation for attenuation changes[21], Arthur et al. initially proposed the change in backscattered energy (CBE) technique and successively used in 1D[22], 2D[23, 24], and 3D[25] for noninvasive quantification of small temperature variations (37 – 50°C), without tissue structural coagulation, as typical of hyperthermia.

Currently, CBE imaging has been utilized in the monitoring of RF[16], MW[17], and HIFU[26] ablations. However, CBE imaging may be limited by the outliers in the boundary due to the estimation procedure within a fixed-size resolution cell[27, 28] and the echo shift artifacts from thermal expansion and contraction, changes in the speed of sound, and concurrent desiccation during heating targets[25, 29] may affect the stability and robustness of CBE estimation and need to be considered in CBE monitoring of ablative thermal therapy.

HIFU and focused ultrasound (FUS) technologies, due to unique properties of ultrasound energy propagation in tissue, have been demonstrated to provide deep and precise control of thermal ablation from extracorporeal or endocavity devices coupled with MR[8, 9] or US[30, 31] real-time monitoring. Similarly, CBUS in an intraluminal or percutaneous form can deliver energy directly adjacent to or from within body lumens, to achieve targeted localization of thermal ablation deep within the body[5, 6]. Interstitial CBUS typically consists of linear arrays of tubular ultrasound transducers, which can be sectored to shape the acoustic energy in the angular expanse, and at high-intensities can produce thermal coagulation zones extending 3 – 4 cm diameter, and of variable length according to the dimensions of the array[32]. However, temperature-time heating strategies and tissue heating dynamics from CBUS can be quite different than the other energy modalities, which present challenges for US or CBE image monitoring of CBUS therapy. In RF, MW, and HIFU ablations with typical high-power and high-temperature settings, coagulated tissues exhibit heat desiccation, boiling, and cavitation bubbles[33–36] and are surrounded by a narrow rim of moderately damaged tissue[36], which present hyperechoic signals and obvious dynamic changes in US images and parametric images[33–36]. In CBUS ablation with lower applied power and relatively lower maximum temperatures, ultrasound visualization of dynamic changes in target tissues can be limited, especially in order to cover an extensive broad lower temperature region extending to the outer 50 – 52 °C boundary of the thermal lesion [37, 38]. Thus, currently US methods to monitor CBUS are challenged by low contrast and sensitivity to tissue changes encountered in the periphery and outer boundary of the thermal lesion during the procedure, which makes practical monitoring and verification of thermal tissue damage difficult. Although the feasibility of using CBE to specifically monitor CBUS thermal therapy is unknown and has not been characterized in prior studies, the inherent challenges in US monitoring likely limit the robustness and contrast of standard CBE techniques for this purpose.

Therefore, the objective of this study is to investigate the feasibility of CBE-guided directional CBUS thermal therapy, and to propose a novel CBUS-based multi-spatiotemporal compounding CBE (MST-CBE) imaging approach that offers enhanced robustness and contrast and lesion determination. Tissue-modification-ratio (TMR) is introduced to determine the robustness and contrast of MST-CBE monitoring approach for CBUS thermal therapy. Bland-Altman analyses between *ex vivo* tissue sections and MST-CBE images are incorporated to evaluate the agreement of ground truths and estimated ablation zones and the efficiency of the proposed MST-CBE approach in monitoring CBUS thermal therapy.

II. Experiments

A. Directional catheter-based ultrasound applicator

In this study, a directional 180°-CBUS applicator (Fig. 1a) was used to deliver US energy and generate discrete zones of temperature elevation and subsequent thermal ablation and coagulation in order to evaluate our CBE monitoring approach. The applicators were designed to deliver hyperthermia or thermal ablation and allowed dynamic control of the heating along the length and angular sectoring if desired to precisely control thermal therapy to conform to the target volume while directing energy away from sensitive or non-targeted tissues[32]. Typical configurations, as used here, consist of tubular PZT-4 piezoceramic transducers (1.5 mm OD × 10 mm length, ~7.6 MHz, 180° active sector, ~150° directional heated zone) within a plastic implant catheter (13-gauge, 2.4 mm). Temperature-controlled water is circulated within the catheter for coupling and control of the interface temperature. The axial and rotational position of the therapy transducers can be adjusted within the catheter and directed for each experimental setup as described below.

B. Ex vivo experiments

Thermal ablation of *ex vivo* homogeneous tissue samples without large vessels and sinuses using CBUS devices while under concurrent ultrasound monitoring was used to investigate the feasibility and performance of the proposed method (Fig. 1 b). Sections ($n = 15$) of degassed chicken muscle ("chicken breast tissue"), each cut to a volume of ~ 5.4 cm × 5.4 cm × 4.8 cm and placed in a custom 3D printed sample holder, were positioned in a stereotactic frame for aligning the CBUS applicator with the endorectal curvilinear ultrasound imaging probe. Markers and points of separation in the tissue sample holder were used post-procedure to align slicing the tissue in cross-section for visual inspection of the thermal coagulation and comparison to the imaging. The combination of the aligned probe, template and sample case were designed to best ensure the US imaging plane, central zone of thermal therapy, and tissue cross-section are on the same plane. The template and sample case were printed by a 3D printer (Model: M200, Zortrax, Poland) using polymer acrylonitrile-butadiene-styrene. For each test case, the fixture and frame were immersed within a 37 °C temperature regulated tank of degassed water, and the tissue was allowed to come to thermal equilibrium. Acoustic absorbers were placed on the inner walls of the water tank to minimize the potential effects of reflection on the imaging and acoustic field[39, 40].

The CBUS applicator was inserted into the tissue samples through a custom template and centered within the sample, ~ 3 cm deep from the imaging probe, with directional energy propagation oriented approximately lateral in these transverse images. The applicator cooling flow was regulated at 15 – 20 ml/min at 37 °C, and ultrasonic power was delivered using an Advanced Surgical RF generator (Model: 500–009, Advanced Surgical Systems, Tucson, AZ, USA) with external triggering capabilities. Ultrasound imaging and raw RF data were recorded by an ultrasound imaging research system (Model: Sonix-MDP, Ultrasonix, Richmond, BC, Canada) equipped with a 128-element endorectal curvilinear array probe (Model: BPC 8–4, Ultrasonix, Richmond, BC, Canada; bandwidth of 4 – 8 MHz, curvature radius of 10 mm, view field of 149°).

An arbitrary waveform generator (Model: AFG 3022C, Tektronix, Wilsonville, OR, USA) was used to synchronize and interleave the CBUS therapy power delivery and acquisition of images from the MDP platform (Fig. 1c). During the ablation sequence, a net power of 10 W was delivered to the CBUS applicator at a duty cycle of 95% with a pulse repetition frequency (PRF) of 0.066 Hz. The applied power level of 10 W was selected based upon *ex vivo* and *in vivo* studies, with approximately 150° directional heating patterns extending to about 15 mm radial distance anticipated [32,37,38]. Ultrasound imaging (6.0 cm depth) at five frames and a PRF of 11.1 Hz within a short-time window of 450 ms were acquired during 30 s preheating, power application, and for 3 min of cooling time and synchronized to the short periods of therapy power off. The emitted-pulse frequency of the imaging probe was 5.0 MHz and the sampling frequency of raw RF data was 40 MHz. All samples were divided into three groups according to the different treatment durations of 3, 6.5, and 10 min. The sample number in these groups was 4, 4, and 7, respectively. After the cool-down sequence, each tissue sample holder was removed from the template, and using the guides on the holder the tissue was sliced along the imaging plane. Photos of the gross tissue cross-sections were taken, and the transverse and radial dimensions of the visible ablation zones were measured. Transient temperature changes representative of each group were measured within the peripheral heated zone in a single sample using a four-sensor thermocouple probe (constantan-manganin, 2.5 mm junction separation, 0.4 mm OD, 20 g needle). The temperature probe was oriented parallel to the applicator at a radial distance of approximately 7.1 mm, with the sensor array centered with the transducer segment and the ultrasound imaging plane; the position of the needle sensor is off-center of the maximum heated zone and within a region that best reflects the peripheral region of the thermal lesion and most important to correlate to imaging. Further, the temperature probe was positioned slightly distal to applicator in reference to the ultrasound imaging probe to minimize effects of shadowing in the imaging.

III. Methods

A. CBE theory

US backscattered energy $\mathbb{R}^2$ is determined by the squared envelope data[22]. The envelope $\mathbb{R}$ can be detected by applying the Hilbert transform function to the oscillating raw RF data. $\mathbb{R}^2$ is collectively considered a scale parameter in the Nakagami statistical model in the description of envelope power distribution[41]. The $\mathbb{R}^2$ from particles and tissue constituents has been shown to change as a function of temperature and has formed the basis of techniques for CBE monitoring[22]. Following the technique proposed by Arthur et al., the $\mathbb{R}^2$ at 37°C or baseline prior to thermal therapy can be taken as the reference data and then the ratio of $\mathbb{R}^2$ at each temperature relative to the reference can be calculated to obtain a CBE parameter (η) to characterize the temperature changes in a target tissue[22–25].

$$\eta(T) = 10 \times \log_{10} \frac{\mathbb{R}^2(T)}{\mathbb{R}^2(T_{37°C})} \quad (1)$$

where η is the CBE parameter of each pixel at temperature T and $\mathbb{R}$ is the US envelope data at each pixel, respectively.

B. Multi-spatiotemporal (MST) compounding CBE mapping method

Calculation of CBE through Equation (1) is a pixel-to-pixel algorithm and is highly sensitive to echo shift and transient changes in US backscattered echoes[17], which may result in unstable estimates and small errors. Based on previous studies using a window-to-window scheme with a fixed size[16, 42, 43] and window-modulated compounding method with an adjustable size[27, 28], this study proposes an MST-CBE imaging approach to increase sensitivity and contrast for monitoring specific to CBUS thermal ablation. Figure 2 displays the MST-CBE algorithm flow diagram, as the following four steps:

1. RF data from the curvilinear imaging probe were interpolated three times in the cross direction (θ) using the cubic spline interpolation method to improve the cross-resolution in polar coordinates (θ, r), especially in deep tissue. With the Hilbert transform, envelope data $\mathbb{R}(\theta, r, t)$ were then obtained from the raw RF data.

2. CBE was estimated window-to-window from the $\mathbb{R}(\theta, r, t)$ data, as the following equation:

$$\hat{\eta}\left(\theta_l, r_p, t_{n,i}\right) = 10 \times log_{10} \frac{\sum_{l=w-\frac{W}{2}}^{w+\frac{W}{2}-1} \sum_{p=d-\frac{D}{2}}^{d+\frac{D}{2}-1} \mathbb{R}^2\left(\theta_l, r_p, t_{n,i}\right)}{\sum_{l=w-\frac{W}{2}}^{w+\frac{W}{2}-1} \sum_{p=d-\frac{D}{2}}^{d+\frac{D}{2}-1} \mathbb{R}^2\left(\theta_l, r_p, t_{1,i}\right)} \tag{2}$$

with $i \in [1,5]$, $d \in \left[\frac{D}{2}, H-\frac{D}{2}\right]$, $l \in \left[\frac{W}{2}, L-\frac{W}{2}\right]$,

$$D = \frac{3\lambda}{c} f_s, \tag{3}$$

and

$$W = \frac{3\lambda L}{\varphi r_p} \tag{4}$$

where $\hat{\eta}\left(\theta_l, r_p, t_{n,i}\right)$ is the CBE value at the l-th scan line in the cross direction, the p-th point in the US beam direction, and the i-th frame within the t_n-th short-time window, which is an averaged value within a spatial window of $W \times D$. D and W are the data points of a length of 3λ in the US beam and cross directions, respectively; λ is a wavelength of imaging pulses; f_s is the sampling frequency of raw RF data; c is the sound speed in the tissue; φ is the angle of the curvilinear array probe; and H and L are the total point numbers in the US beam direction and line numbers in the cross direction, respectively. The energy data before thermal therapy at the time of $t_{1,i}$ was taken as the reference data at 37°C.

3. MST-CBE was obtained using the following equation:

$$\overline{\hat{\eta}}(\theta_l, r_p, t_n) = \frac{1}{15}\sum_{i=1}^{5}\sum_{j=1}^{3}\hat{\eta}(M_j, t_{n,i}) \tag{5}$$

with

$$M_j = \begin{bmatrix} \theta_w - j\frac{W}{2}, r_d - j\frac{D}{2} & \cdots & \theta_w + j\frac{W}{2} - 1, r_d - j\frac{D}{2} \\ \vdots & \theta_l, r_p & \vdots \\ \theta_w - j\frac{W}{2}, r_d + j\frac{D}{2} - 1 & \cdots & \theta_w + j\frac{W}{2} - 1, r_d + j\frac{D}{2} - 1 \end{bmatrix} \tag{6}$$

where $\overline{\hat{\eta}}$ is the compounding MST-CBE value within a group of adjustable spatial windows with a range size from 3λ × 3λ to 9λ × 9λ and within the short-time window t_n. These adjustable spatial windows constituted a group of sliding windows with the center (θ_l, r_p) in Equation (2). The center of these adjustable spatial windows moved at one-pixel intervals and the procedures in the second and third steps were repeated in the whole matrix of $\mathbb{R}(\theta, r, t)$. Finally, the MST-CBE values of all pixels in $\mathbb{R}(\theta, r, t)$ were estimated.

4. Two components of absolute and positive CBE were obtained in MST-CBE values $\overline{\hat{\eta}}(\theta, r, t)$, which were denoted by MST-CBE_{abs} and MST-CBE_{pos}, respectively. MST-CBE_{abs} is the total change in backscatter energy and MST-CBE_{pos} is only the positive changes. Absolute and positive $\overline{\hat{\eta}}(x, z, t)$ were reconstructed in the Cartesian coordinates from the polar coordinates. According to a standard color model of 'JET-256', MST-CBE_{abs} and MST-CBE_{pos} contour maps were color-coded to image the changes in deposition energy and coagulation zones within ablation targets during heating.

In addition, the multi-temporal (MT) and multi-spatial (MS) strategies alone were also investigated in CBE estimation, and MT-CBE and MS-CBE calculations were obtained for comparison to the MST-CBE estimation. MS-CBE was calculated using only a single frame ($i = 1$) rather than all frames within the t_n window to calculate CBE in Equation (5). MT-CBE was calculated using only one spatial scale of 3λ × 3λ ($j = 1$) and all frames within the t_n window were used to calculate CBE in Equation (5). Herein, the MT and MS are respectively the temporal and spatial compounding strategies with a less computational cost.

IV. DATA ANALYSIS

A. Contrast evaluations

Tissue-modification ratio (TMR) was used herein to evaluate the image contrast and robustness of the MST-CBE technique, as defined by the following equation:

$$\mathrm{TMR}(t_n) = 20 \times \log_{10}\left[\overline{\mathrm{H}}(t_n)/\overline{\mathrm{H}}(t_1)\right] \tag{7}$$

where $\overline{H}(t_n)$ is the average data of $\overline{\hat{\eta}}$ within a region-of-interest (ROI) at the n-th short-time window obtained from MST-CBE. $\overline{H}(t_1)$ is the corresponding average data within the same ROI at the first short-time window, which was normal tissue without heating and without ablation, and was known as the background data during TMR calculation. The ROI size was fixed as ~ 6 mm × 6 mm. We investigated the TMR changes within the center (ROI-1) and on the boundary of ablation zones (ROI-2), respectively.

For further comparison, conventional B-mode images, Nakagami shape parametric images (NK_m)[27, 28], Nakagami scale parametric image (NK_Ω)[27, 28], and conventional CBE images[16, 17] were also determined, and together with the MT-CBE and MS-CBE images, were compared to images of the MST-CBE technique. Thus, H in the Equation (7) could be replaced by the corresponding average data within the same ROI obtained from B-mode, NK_m, NK_Ω, CBE images, and the above images using MT and MS strategies, respectively, to calculate their TMR. Note that all group data from all samples using the above monitoring techniques were normalized to ensure all data were at the same dynamic range during the comparison.

B. Evaluations of ablation dimensions and area

Ground truth measurements of lesion dimensions and calculated areas of ablation zones in the tissue cross-sections as obtained from the three groups were used in guiding the corresponding estimations with the MST-CBE images. The lesion dimensions, based upon visible zones of thermal coagulation in tissue section photos, were measured as the maximum radial depth from the applicator surface, and as the maximum transverse distance to define the width of the directional lesion. Then, the areas of ablation zones were calculated by using an ellipse area equation based on the above-measured lesion dimensions.

To stably and accurately estimate the transverse and radial dimensions and ablation areas and match the regular contours in the tissue cross-sections, the MST-CBE_{abs} and MST-CBE_{pos} maps were fitted using a sixth-order polynomial function in the axial and lateral imaging direction[16]. Two threshold values in the treatment duration of 3, 6.5, and 10 min were respectively selected to crop the fitted MST-CBE_{abs} and MST-CBE_{pos} maps, and the corresponding pixel numbers within the ablation zones were obtained. Based on the actual physical size of pixel, the transverse and radial dimensions and ablation areas could be estimated at the last frame obtained during the last portion of sonication.

Bland-Altman analysis and agreement analysis between ground truth measurements and estimated ablation dimensions depicted by MST-CBE images were performed to optimize the selection of threshold values. The correlation coefficient (R^2), bias, and standard deviation (STD) between them were calculated, respectively. To minimize the deviation of ablation areas between the tissue section measurements and MST-CBE image estimations, the threshold values were coarse-to-fine optimized through an iterative process according to the agreement and Bland-Altman analyses. The threshold values were tuned to a range of 0.80 – 0.98 with a small interval from 0.01 to 0.001, and two optimized threshold values were obtained for area estimation using MST-CBE_{abs} and MST-CBE_{pos} images, respectively.

C. Statistical analysis

The mean value and standard deviation of the measurements and determinations were determined, and statistical comparisons were performed using paired-sample t-tests. All post-processing were performed using MATLAB (#2019b, MathWorks Inc., Natick, MA, USA) on a workstation (system: Win 10, processor: Intel Xeon CPU E5-2620v4@2.1 GHz, RAM: 128 GB; Dell Computer Inc., USA).

V. Results

A. B mode, Nakagami parametric images

Figures 3 and 4 display a typical case and comparison of normalized B-mode, NK_m, and NK_Ω parametric images pre-treatment and during thermal therapy with the 180°-CBUS applicator, respectively. Locations of the applicator and thermocouple probe are marked with a small yellow circle (ϕ = 2.4 mm) and a red point in Fig. 3, respectively. The approximate direction and zone of thermal therapy are demarcated by the larger circle (ϕ = 12 mm) offset to the side of the applicator in Fig. 3. For all cases, the maximum temperatures at the periphery of the coagulated zone measured via thermocouple at 10 min ranged from 52 °C to 56.5 °C. However, these changes in temperature elevation and ablation zones during CBUS heating could not be imaged or depicted by either change in the B-mode or Nakagami parametric ultrasound images.

B. CBE and MST-CBE maps

Figure 5 shows the comparison of normalized absolute CBE images of CBE_{abs}, $MT\text{-}CBE_{abs}$, $MS\text{-}CBE_{abs}$, and $MST\text{-}CBE_{abs}$ during pre-therapy and thermal therapy using the 180°-CBUS applicator for the same case of Figs. 3–4. Figure 6 indicates the corresponding normalized positive CBE images of CBE_{pos}, $MT\text{-}CBE_{abs}$, $MS\text{-}CBE_{abs}$, and $MST\text{-}CBE_{abs}$. Compared with B-mode and Nakagami parametric imaging techniques in Figs. 3 and 4, all CBE images in Figs. 5 and 6 observed changes associated with deposition energy and coagulation zones within target tissues during CBUS heating, and were more significant when MS-CBE and MST-CBE techniques were used.

C. TMR of CBE images

Figure 7 shows the examples of mean TMR curves as a function of time over the treatment duration in seven monitoring methods, namely, B-mode, NK_m, NK_Ω, CBE_{abs}, CBE_{pos}, $MS\text{-}CBE_{abs}$, and $MS\text{-}CBE_{pos}$ techniques, and in the corresponding seven methods combined with MT estimation strategy including $MST\text{-}CBE_{abs}$ and $MST\text{-}CBE_{pos}$ techniques. These TMR curves were calculated from the ROI-1 within the center of ablation zones as depicted in Fig. 5. In these examples of TMR curves, $MS\text{-}CBE_{pos}$ and $MST\text{-}CBE_{pos}$ techniques produced the maximum TMR values of 42.52 dB and 42.55 dB during the whole treatment duration of 10 min in Figs.7a and 7b, respectively, which were consistent with the changes in deposition energy in the targets obviously characterized in Figs. 5 and 6.

Figure 8 summarizes the statistical analysis of the mean and maximum TMR values within ROI-1 as varied with treatment duration of all samples for the seven monitoring methods with and without MT estimation strategy. Table 1 shows the comparison of maximum TMR

values between MST-CBE and other techniques. Table 2 shows the comparison of mean TMR values of CBE techniques with and without MS, MT, and MST estimation strategies. These results indicate that all CBE techniques exhibited larger TMR than B-mode, NK_m, and NK_Ω images. All absolute and positive MS-CBE images had larger TMR values than the corresponding components of MT-CBE and conventional CBE images. MST-CBE images exhibited the greatest TMR when compared to all other six techniques. Similar results were observed in the TMR curves and the corresponding statistical analysis within ROI-2 on the boundary of ablation zones as depicted in Fig. 5. Moreover, the mean values of the TMR curves of MST-CBE_{abs} and MST-CBE_{pos} within ROI-2 on the boundary were 3.25 ± 1.22 dB ($p < 0.05$) and 4.19 ± 3.64 dB ($p = 0.06$) larger than those within ROI-1 in the center of the ablation zones, respectively.

D. Ablation sizes estimated from MST-CBE images

The MST-CBE images exhibited higher contrast of all techniques, and thus were selected to estimate the transverse and radial lesion dimensions and ablation area cross-sectional areas. Figure 9 demonstrates the ablation zones in the tissue sections and the corresponding estimates from fitted MST-CBE images for treatment duration of 3, 6.5, and 10 min, respectively. As delineated by the translucent color areas marked on the corresponding B mode images in Fig. 9, the ablation cross-sectional areas were estimated from fitted MST-CBE_{abs} images in Fig. 9b based on a threshold value of 0.883 and from fitted MST-CBE_{pos} images in Fig. 9c based on a threshold value of 0.845. The optimizing and tuning of threshold values were discussed in the VI.F subsection. With the increase in treatment duration from 3 to 10 min, the estimated ablation areas also increased and nearly matched the corresponding increase of coagulation zones in the tissue sections. Figure 10 indicates the measured and estimated transverse and radial dimensions and areas within the ablation zones of all *ex vivo* tissue samples. The quantifications of agreement and Bland-Altman analyses between all measured and estimated transverse and radial dimensions in the ablation zones are shown in Figs. 11a and 11b, respectively. For all cases, the correlation coefficient R^2 value, bias, and STD of transverse lesion dimensions estimated in the MST-CBE_{abs} images were 0.75 ($p < 0.005$), −0.56 mm, and 1.03mm, respectively. The R^2 value, bias, STD of radial lesion dimensions estimated in the MST-CBE_{pos} images were up to 0.93 ($p < 0.001$), 1.77 mm, and 0.75 mm, respectively. Figure 11c displays the corresponding analyses of the areas within the ablation zones of all samples. The R^2 value, bias, STD of ablation areas estimated the MST-CBE_{pos} images were 0.91 ($p < 0.001$), −0.72 mm^2, and 8.18 mm^2, respectively. These results illustrate that the proposed MST-CBE monitoring method with high TMR has enough sensitivity to depict the shape and changes in ablation size during directional CBUS thermal therapy.

VI. DISCUSSION

A. CBUS-based B-mode and Nakagami parametric images

This study showed that US-based Nakagami parametric imaging performed poorly in characterizing and monitoring tissue changes during CBUS thermal therapy delivered with standard treatment delivery strategies. This is in contrast to the successful applications of Nakagami imaging for monitoring RF, microwave, and HIFU ablations using methods

developed and evaluated in recent years [20, 33–36]. In those previous studies, thermal coagulation zones were produced using either high intensities from focused transducers (>200W/cm^2) for short duration sonications of typical of HIFU ablation[20, 33, 34]; or applied applicator power levels of 50 W – 100 W to 1 – 2 cm radiating aperture for 10 – 15 min treatment time typically applied in RF and microwave ablation[35, 36]. Consequently, temperatures within target tissues rapidly increased to 65 – 110 °C[36], hyperechoic zones appeared in the US images because heat desiccation, boiling, cavitation, and numerous gas bubbles were induced by ablations[33–36]. Thus, in this high power and high temperature setting, dynamic changes in target tissues were observed in raw envelope data, B-mode echoes, and Nakagami parametric images during RF[35, 36], microwave[20], and HIFU[20, 33, 34] ablations. In consideration of CBUS therapy, power application is typically 10 – 18 W per cm transducer segment, with intensities less than 10 W/cm^2 during power applications of 5 – 15 min duration. The maximum temperatures obtained in the central heating zone close to the applicator can approach approximately 55 to 90 + °C[37, 38] depending upon the sonication strategy and target tissue properties. As shown herein, temperature measured in the peripheral coagulation zone in proximity to the central target rapidly increased to 52 – 56.5 °C, which did not produce boiling, cavitation bubbles or hyperechoic signals in the B-mode images (Fig. 3), nor were any significant changes to the corresponding Nakagami parametric images noted (Fig. 4). These results are suggestive that the B mode and Nakagami parametric imaging, as shown effective for the high power and high thermal dose ablative therapies, are not sufficient for monitoring the more diffuse boundaries of thermal ablation therapy delivered using CBUS devices. Although Nakagami parametric applications are highly sensitive in characterizing the statistical distribution of backscattered echoes [33–36], the successful implementation for monitoring CBUS thermal therapy has been constrained due to the above reasons.

B. MST-CBE v.s. other techniques

This study proposed and implemented an MST-CBE imaging approach for characterizing and monitoring the dynamic changes within target tissues during CBUS thermal therapy with significantly better contrast and sensitivity than standard B-mode and Nakagami parametric imaging. It illustrated that the CBE and the proposed MST-CBE methods could depict thermal therapy regions at a low threshold value of thermal dose or exposure, notably considering the typical lower energy deposition and temperatures associated with CBUS. These comparisons verified that the CBE detection theory is feasible in monitoring thermal therapy using a directional CBUS applicator, which is similar to the applications of CBE monitoring applied in the RF[16], microwave[17], and HIFU[26] ablations.

In this study, we explored three CBE strategies, namely, the MS, MT, and MST approaches, which significantly improved the contrast of conventional CBE techniques. Herein, an order of improvement in TMR was MST > MS > MT strategies. The MST strategy maximally exploited the sensitivity of CBE estimation and demonstrated the highest contrast and robustness during the monitoring of CBUS thermal therapy. These results suggest that the proposed MST-CBE method has potential in monitoring and assessing not only thermal ablation but possibly hyperthermia applications, which typically apply milder

temperature elevation (40 – 45 °C) as typically applied as an adjunct to radiation therapy and chemotherapy [29, 38].

C. Influences of echo shift

The proposed MST strategy integrated the advantage of the MS strategy in suppressing outliers induce by echo shift and the ability of the MT strategy in restraining artifacts induced by slight tissue motion and contraction during thermal therapy. CBE estimation based on the pixel-to-pixel ratio in the spatial scale is sensitive to echo shift induced by thermal expansion and changes in the speed of sound during thermal therapy[22–25], and due to pixel-to-pixel mismatching could result in inaccurate estimates. These limitations, similar to the limitation in Nakagami parameters[27, 28], might affect the robustness and stability of CBE estimation. Considering these limitations, Arthur et al. investigated various motion tracking, compensation, and phase correction algorithms to suppress the influences of echo shift on CBE estimation[25, 29]. However, Tsui et al. indicated that motion tracking and correction may be unnecessary when CBE is only used to depict temperature changes without induced irreversible coagulation zones [17]. Trobaugh et al. noticed the influences of spatial size on the ability to suppress echo shift artifacts during pixel-to-pixel CBE estimation and used a 3 × 3 running average filter to smooth the CBE values[42]. Xia et al.[43] and Zhang et al.[16] initially used window-to-window CBE estimation schemes to replace the pixel-to-pixel scheme without additional motion compensation or phase correction processing. However, when a fixed window size was used[16, 42, 43], the echo shift artifacts were not completely removed, the outliers were produced at the boundary of windows, and the robustness and stability of CBE estimation remained limited. These limitations result in production of discontinuous and alternating positive/negative shading features within CBE images[17], and thus positive and negative CBEs were studied separately as a means for reduction of these shading features[16]. Therefore, based on previous studies using a window-modulated compounding method with an adjustable size[27, 28], the MS strategy was used in the window-to-window MST-CBE estimation scheme to remove the outliers and improve the smoothness of CBE images. In fact, the MS estimation strategy can suppress spatial clutter and stabilize CBE estimation.

D. Influences of target motion and contraction

Additionally, CBE estimation is affected by transient motion of target tissues induced by respiratory motion, cardiac impulse, therapy applicator shift, and imaging probe movement[17]. Given in our study that the template was used in fixing the locations of the therapy applicator and imaging probe, the influences of relative motions were minimized during the thermal therapy test sequences. Moreover, the US imaging sequence and thermal therapy sequence with a low power were designed in this study, and the five US frames were recorded within a short-time window of 450 ms, which made it possible to perform the MT strategy. Therefore, the MT strategy was integrated into the proposed MST-CBE estimation scheme as a means to suppress artifacts induced by slight tissue contraction due to the protein denaturation and thermal coagulation during heating, and to reduce the distortions induced by a small and rapid swing of 180°-CBUS applicator when power on and off was switched. The equalization effect in the MT strategy suppresses the artifacts and distortions induced by target motion and improves the robustness of CBE estimation. However, the

advantages of MT strategy in MST-CBE estimation was possibly underestimated in our work due to no target movements induced by respiratory motion and cardiac impulse, since these were *ex vivo* validations with a relatively low rate of temperature change and protein coagulation within this short-time window. Thus, improvement in TMR in the MT strategy was smaller than the corresponding improvement in the MS strategy. Therefore, the proposed MST-CBE monitoring technique combined the MS and MT strategies and integrated their respective advantages, which had the ability to suppress the pixel-to-pixel mismatching and outliers induced by echo shift and reduce the artifacts and distortions induced by target motion during a long-time CBUS thermal therapy. The MST-CBE monitoring technique demonstrated am improvement to robustness and stability of CBE estimation.

E. Threshold determination of MST-CBE for ablation area estimation

Image-based monitoring and final assessment of thermal ablation zones not only provides a means to verify completion of the thermal therapy procedure but also may provide feedback on treatment progression, thermal parameters, and energy control, each of which are key parameters required for precise thermal therapy[5–7, 18]. As shown in Figs. 10a and 10b, the transverse dimensions were slightly underestimated but the radial dimensions were slightly overestimated, most likely since the MST-CBE maps were first fitted in the axial direction and then in the lateral direction in relation to the ultrasound imaging. Thus, to determine the optimal thresholds to apply in MST-CBE images to denote tissue change areas corresponding to thermal ablation areas, a direct comparison was made to the measured ablation areas rather than dimensions while iteratively linearly adjusting threshold values to obtain the best fit. The average estimated ablation areas determined from the measured dimensions over the three experimental groups were consistent with the ground truths of measured areas in Fig. 10c. Owing to the same reason, the biases of the estimated areas in Bland-Altman analysis in Fig. 11c were smaller than those of estimated transverse and radial lesion dimensions in Figs. 11a and 11b.

According to the agreement and Bland-Altman analyses, the threshold values were coarse-to-fine optimized to minimize the deviation of ablation areas between the measured in tissue sections and estimated from MST-CBE images. Two threshold values of 0.883 and 0.845 were finally selected for area estimation using $\text{MST-CBE}_{\text{abs}}$ and $\text{MST-CBE}_{\text{pos}}$ images, respectively. Based on these threshold values, the R^2 value of the ablation areas estimated from the $\text{MST-CBE}_{\text{pos}}$ images was up to 0.91 ($p < 0.001$) and larger than that from the $\text{MST-CBE}_{\text{abs}}$ images. However, the biases of the estimated dimensions and areas from the $\text{MST-CBE}_{\text{abs}}$ images were smaller than those from the $\text{MST-CBE}_{\text{pos}}$ images because the $\text{MST-CBE}_{\text{abs}}$ covered the negative component and the $\text{MST-CBE}_{\text{pos}}$ only had the positive component. Thus, the optimal threshold values should consider the balance between the multi-parametric quantifications in the agreement analysis and Bland-Altman analysis. The proposed MST-CBE imaging technique has been shown to monitor the dynamic changes in tissue structure and heating due to energy deposition and response within target tissues and also depict the ablation areas during thermal therapy. Thus, the MST-CBE technique has potential for real-time accurate monitoring and evaluation for thermal therapy using directional CBUS applicators[6, 18].

F. Considerations toward future work

In this work the MST-CBE approach was demonstrated feasible for monitoring thermal ablation using CBUS devices, but validation was limited to discrete time points during the ablation process and 2D images were obtained within a single type of tissue in the *ex vivo* setting using a 1D imaging probe. In consideration of further advancing the MST-CBE approach, evaluations in different tissues within *ex vivo* and *in vivo* settings can be performed to determine tissue specific performance indices, along with more comprehensive investigations of variations due to different applied power-time and temperature trajectories (applicator power and time). These evaluations would be most important in highly vascularized and heterogeneous tissue regions, where the need of higher powers and subsequently higher temperatures near the applicator may generate larger zones of desiccated tissue and sharper thermal gradients at the periphery of the coagulation zone, and could impact the ability of the MST approach to accurately track the coagulation zone. In addition, the effect of shadowing [16] of distant imaging from the CBUS applicator on the MST-CBE tissue characterization was not directly investigated in the present study. The influence of catheter shadowing may have been partially suppressed since directional CBUS applicators were used at an angle of energy delivery without along the US beam direction, whereas 360° or other active sector angles along with longer or multiple transducer sonication may behave differently. For the moderate power levels of CBUS applied in the current *ex vivo* study, the errors induced by slight tissue contraction during lower maximum temperature heating were suppressed by MST-CBE strategy with no artifacts induced by target movements; however, the errors possibly induced by higher power levels and greater temperature elevations may generate large amounts of tissue contraction and target motion especially in *in vivo* conditions which should be explored. Finally, in the proposed MST-CBE approach and analysis was performed off-line, whereas to be practical for real-time monitoring, the algorithm and processing pipeline can be integrated to GPU processing, and modified to balance computational efficiency and imaging quality specific to target tissues and applications.

VII. Conclusion

This study proposed an ultrasonic MST-CBE imaging method to monitor thermal therapy and ablation using directional CBUS applicators. The proposed method demonstrated the feasibility of CBE detection theory in monitoring CBUS thermal therapy, and the addition of the MST approach significantly improved the CBE imaging contrast and robustness as evaluated by TMR. Validations within *ex vivo* tissue illustrated that the MST-CBE method could not only monitor the dynamic changes in tissue structure and temperature response due to thermal therapy with a high TMR, but can also depict the dimensions and cross-sectional areas of the ablation zones achieved in targeted tissues. The proposed MST-CBE method is feasible for providing a means to monitor and provide feedback to control and validate thermal therapy using directional CBUS applicators, with additional development and integration warranted.

Supplementary Material

Refer to Web version on PubMed Central for supplementary material.

Acknowledgments

This work was supported by NIH grant R01CA230323 and R01EB025990.

Reference

[1]. Chu KF, and Dupuy DE, “Thermal ablation of tumours: biological mechanisms and advances in therapy,” Nat Rev Cancer, vol. 14, no. 3, pp. 199–208, 2014. [PubMed: 24561446]

[2]. Zimmerman M, and Busuttil RW, “Long-term efficacy of percutaneous thermal ablation for patients with recurrent hepatocellular carcinoma,” Nat Clin Pract Gastr, vol. 3, no. 5, pp. 250–251, 2006.

[3]. Pinder LFet al. , “Thermal ablation versus cryotherapy or loop excision to treat women positive for cervical precancer on visual inspection with acetic acid test: pilot phase of a randomised controlled trial,” Lancet Oncol, vol. 21, no. 1, pp. 175–184, 2020. [PubMed: 31734069]

[4]. Decadt B, and Siriwardena AK, “Radiofrequency ablation of liver tumours: systematic review,” Lancet Oncol, vol. 5, no. 9, pp. 550–560, 2004. [PubMed: 15337485]

[5]. Diederich CJ, “Thermal ablation and high-temperature thermal therapy: overview of technology and clinical implementation,” Int J Hyperther, vol. 21, no. 8, pp. 745–753, 12. 2005.

[6]. Salgaonkar VA, and Diederich CJ, “Catheter-based ultrasound technology for image-guided thermal therapy: Current technology and applications,” Int J Hyperther, vol. 31, no. 2, pp. 203–215, 2. 2015.

[7]. Goldberg SN, Gazelle GS, and Mueller PR, “Thermal ablation therapy for focal malignancy: a unified approach to underlying principles, techniques, and diagnostic imaging guidance,” Am J Roentgenol, vol. 174, no. 2, pp. 323–331, 2000. [PubMed: 10658699]

[8]. Holbrook ABet al. , “Real-time MR thermometry for monitoring HIFU ablations of the liver,” Magn Reson Med, vol. 63, no. 2, pp. 365–373, 2010. [PubMed: 19950255]

[9]. Enholm JKet al. , “Improved volumetric MR-HIFU ablation by robust binary feedback control,” IEEE T Biomed Eng, vol. 57, no. 1, pp. 103–113, 2009.

[10]. Huang Pet al. , “Folic acid-conjugated silica-modified gold nanorods for X-ray/CT imaging-guided dual-mode radiation and photo-thermal therapy,” Biomaterials, vol. 32, no. 36, pp. 9796–9809, 2011. [PubMed: 21917309]

[11]. Purdie T, Sherar M, and Lee TY, “The use of CT perfusion to monitor the effect of hypocapnia during laser thermal therapy in a rabbit model,” Int J Hyperther, vol. 19, no. 4, pp. 461–479, 2003.

[12]. Owen Net al. , “Dual-mode transducers for ultrasound imaging and thermal therapy,” Ultrasonics, vol. 50, no. 2, pp. 216–220, 2010. [PubMed: 19758673]

[13]. Subramanian Set al. , “In vivo thermal ablation monitoring using ultrasound echo decorrelation imaging,” Ultrasound Med Biol, vol. 40, no. 1, pp. 102–114, 2014. [PubMed: 24239361]

[14]. Mast TDet al. , “Treatment of rabbit liver cancer in vivo using miniaturized image-ablate ultrasound arrays,” Ultrasound Med Biol, vol. 37, no. 10, pp. 1609–1621, 2011. [PubMed: 21821349]

[15]. Seo CHet al. , “Thermal strain imaging: a review,” Interface Focus, vol. 1, no. 4, pp. 649–664, 2011. [PubMed: 22866235]

[16]. Zhang Let al. , “Ultrasound single-phase CBE imaging for monitoring radiofrequency ablation,” Int J Hyperther, vol. 35, no. 1, pp. 548–558, 2018.

[17]. Tsui PHet al. , “Using ultrasound CBE imaging without echo shift compensation for temperature estimation,” Ultrasonics, vol. 52, no. 7, pp. 925–935, 9, 2012. [PubMed: 22472015]

[18]. Ahmed Met al. , “Image-guided tumor ablation: standardization of terminology and reporting criteria-a 10-year update,” Radiology, vol. 273, no. 1, pp. 241–260, 2014. [PubMed: 24927329]

[19]. Byra Met al. , “Temperature monitoring during focused ultrasound treatment by means of the homodyned K distribution,” Acta Physica Polonica A, vol. 131, no. 6, pp. 1525–1528, 2017.

[20]. Zhang Set al. , “Ex vivo and in vivo monitoring and characterization of thermal lesions by high-intensity focused ultrasound and microwave ablation using ultrasonic Nakagami imaging,” IEEE T Med Imaging, vol. 37, no. 7, pp. 1701–1709, 2018.

[21]. Tyréus PD, and Diederich C, “Two-dimensional acoustic attenuation mapping of high-temperature interstitial ultrasound lesions,” Phys Med Biol, xvol. 49, no. 4, pp. 533, 2004. [PubMed: 15005163]

[22]. Arthur RMet al. , “Noninvasive temperature estimation based on the energy of backscattered ultrasound,” Med Phys, vol. 30, no. 6, pp. 1021–1029, 6. 2003. [PubMed: 12852524]

[23]. Arthur RMet al. , “Temperature dependence of ultrasonic backscattered energy in motion compensated images,” IEEE T Ultrason Ferroelectr Freq Control, vol. 52, no. 10, pp. 1644–1652, 10. 2005.

[24]. Arthur RMet al. , “In vivo change in ultrasonic backscattered energy with temperature in motion-compensated images,” Int J Hyperther, vol. 24, no. 5, pp. 389–398, 8. 2008.

[25]. Arthur RMet al. , “3-D in vitro estimation of temperature using the change in backscattered ultrasonic energy,” IEEE T Ultrason Ferroelectr Freq Control, vol. 57, no. 8, pp. 1724–1733, 8. 2010.

[26]. Yang Ket al. , “Frequency-domain CBE imaging for ultrasound localization of the HifU focal spot: a feasibility study,” Sci Rep-Uk, vol. 10, no. 1, pp. 1–10, 2020.

[27]. Wang Det al. , “Numerical and experimental investigation of impacts of nonlinear scattering encapsulated microbubbles on Nakagami distribution,” Med Phys, vol. 46, no. 12, pp. 5467–5477, 12. 2019. [PubMed: 31536640]

[28]. Tsui PHet al. , “Window-modulated compounding Nakagami imaging for ultrasound tissue characterization,” Ultrasonics, vol. 54, no. 6, pp. 1448–1459, 2014. [PubMed: 24835004]

[29]. Arthur RMet al. , “Non-invasive estimation of hyperthermia temperatures with ultrasound,” Int J Hyperther, vol. 21, no. 6, pp. 589–600, 9. 2005.

[30]. Rabkin BA, Zderic V, and Vaezy S, “Hyperecho in ultrasound images of HIFU therapy: involvement of cavitation,” Ultrasound Med Biol, vol. 31, no. 7, pp. 947–956, 2005. [PubMed: 15972200]

[31]. Vaezy Set al. , “Real-time visualization of high-intensity focused ultrasound treatment using ultrasound imaging,” Ultrasound Med Biol, vol. 27, no. 1, pp. 33–42, 2001. [PubMed: 11295268]

[32]. Nau W, Diederich C, and Burdette E, “Evaluation of multielement catheter-cooled interstitial ultrasound applicators for high-temperature thermal therapy,” Med Phys, vol. 28, no. 7, pp. 1525–1534, 7. 2001. [PubMed: 11488586]

[33]. Han Met al. , “Nakagami-m parametric imaging for characterization of thermal coagulation and cavitation erosion induced by HIFU,” Ultrason Sonochem, vol. 45, pp. 78–85, 3. 2018. [PubMed: 29705328]

[34]. Zhang Set al. , “Enhanced lesion-to-bubble ratio on ultrasonic Nakagami imaging for monitoring of high-Intensity focused ultrasound,” J Ultras Med, vol. 33, no. 6, pp. 959–970, 2014.

[35]. Zhou Zet al. , “Monitoring radiofrequency ablation using real-time ultrasound Nakagami imaging combined with frequency and temporal compounding techniques,” Plos One, vol. 10, no. 2, pp. e0118030, 2. 2015. [PubMed: 25658424]

[36]. Wang CYet al. , “Monitoring radiofrequency ablation with ultrasound Nakagami imaging,” Med Phys, vol. 40, no. 7, pp. 072901, 7. 2013. [PubMed: 23822452]

[37]. Prakash P, and Diederich CJ, “Considerations for theoretical modelling of thermal ablation with catheter-based ultrasonic sources: Implications for treatment planning, monitoring and control,” Int J Hyperther, vol. 28, no. 1, pp. 69–86, 2012.

[38]. Prakash P, Salgaonkar VA, and Diederich CJ, “Modelling of endoluminal and interstitial ultrasound hyperthermia and thermal ablation: Applications for device design, feedback control and treatment planning,” Int J Hyperther, vol. 29, no. 4, pp. 296–307, 2013.

[39]. Wang Det al. , “Influence of guided waves in tibia on non-linear scattering of contrast agents,” Ultrasound Med Biol, vol. 42, no. 2, pp. 561–573, 2016. [PubMed: 26617242]

[40]. Wang Det al. , “Ultrasound contrast plane wave imaging based on bubble wavelet transform: in vitro and in vivo validations,” Ultrasound Med Biol, vol. 42, no. 7, pp. 1584–1597, 2016. [PubMed: 27067280]

[41]. Abdi A, and Kaveh M, “Performance comparison of three different estimators for the Nakagami m parameter using Monte Carlo simulation,” IEEE commun letters, vol. 4, no. 4, pp. 119–121, 4. 2000.

[42]. Trobaugh JWet al. , “A simulation model for ultrasonic temperature imaging using change in backscattered energy,” Ultrasound Med Biol, vol. 34, no. 2, pp. 289–298, 2008. [PubMed: 17935869]

[43]. Xia Jet al. , “An approach for the visualization of temperature distribution in tissues according to changes in ultrasonic backscattered energy,” Comput Math Method M, vol. 2013, pp. 682827, 2013.

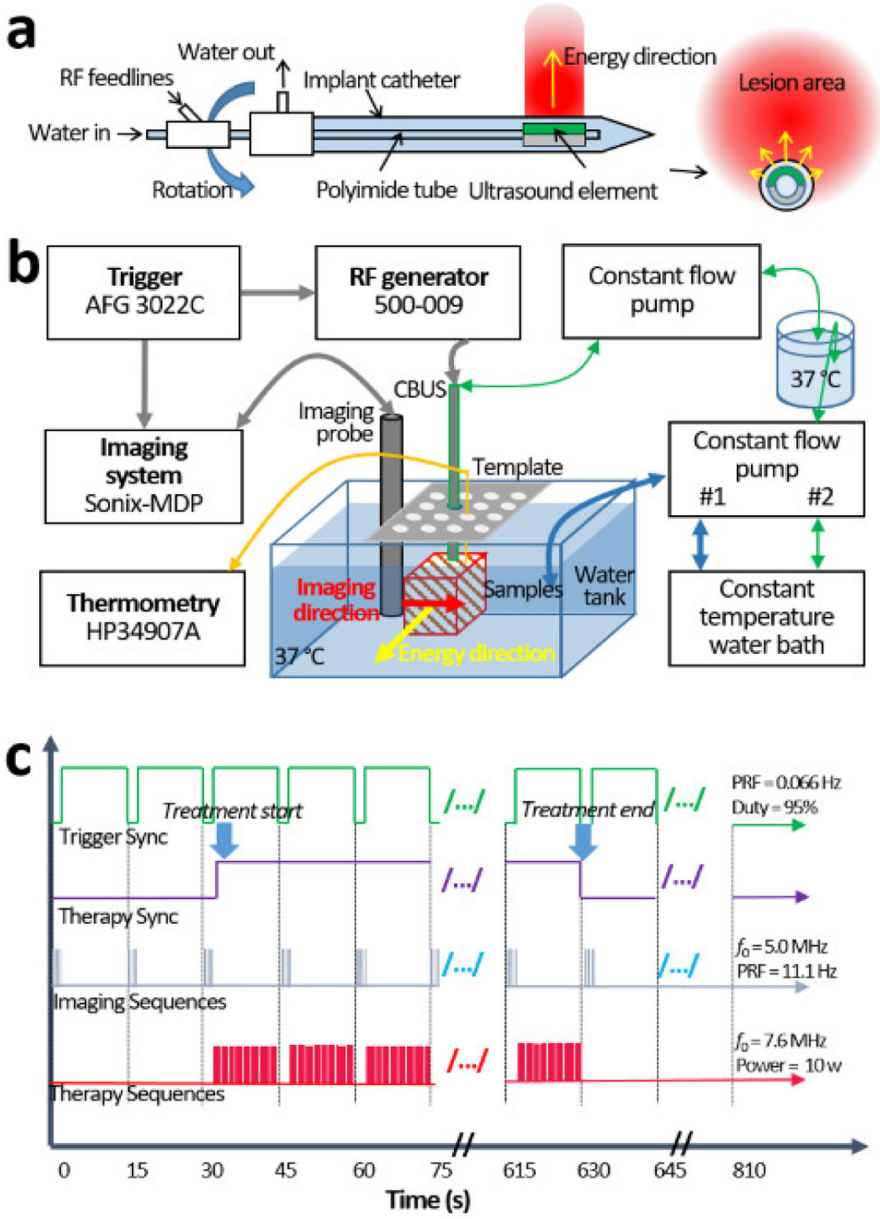

Figure 1.

(Color online) (a) Schematic of percutaneous directional 180° catheter-based ultrasound (CBUS) applicator with depiction of typical thermal lesion shape, (b) *ex vivo* experimental setup of ultrasound monitoring simultaneous to stereotactic placed CBUS thermal therapy, and (c) the corresponding trigger and synchronous sequences for gating imaging and ultrasonic power delivery.

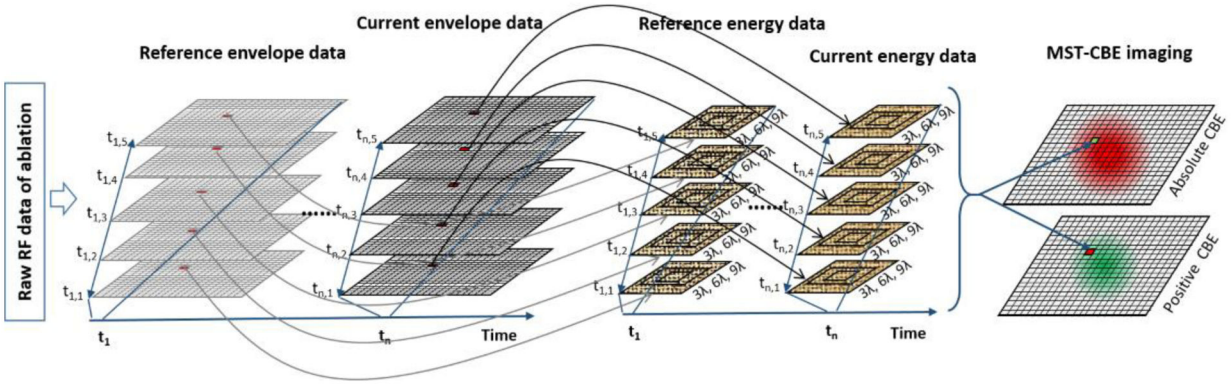

Figure 2.

(Color online) Algorithm flow diagram of the proposed multi-spatiotemporal (MST) compounding ultrasonic change in backscattered energy (CBE) monitoring for thermal therapy using CBUS applicator. After Hilbert transform, envelope data are obtained from raw RF data, spatiotemporal average values of CBE are calculated using MST strategy, and two components of absolute and positive CBE images are finally reconstructed to monitor and assess the thermal therapy.

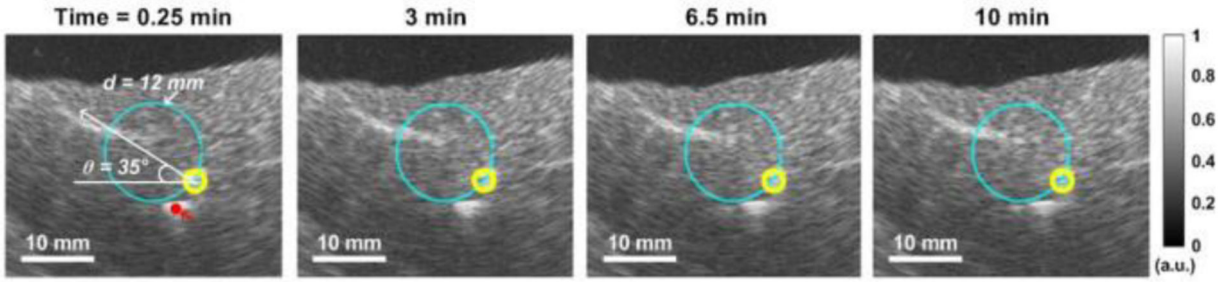

Figure 3.

(Color online) Examples of normalized ultrasound B-mode images during 180°-CBUS thermal therapy depicting in cross-section the applicator position (small yellow circle), angular direction of energy, and approximate zone of ablation (large blue circle). The time sequence of the images is the pre-therapy (0.25 min), and during heating at 3, 6.5, and 10 min.

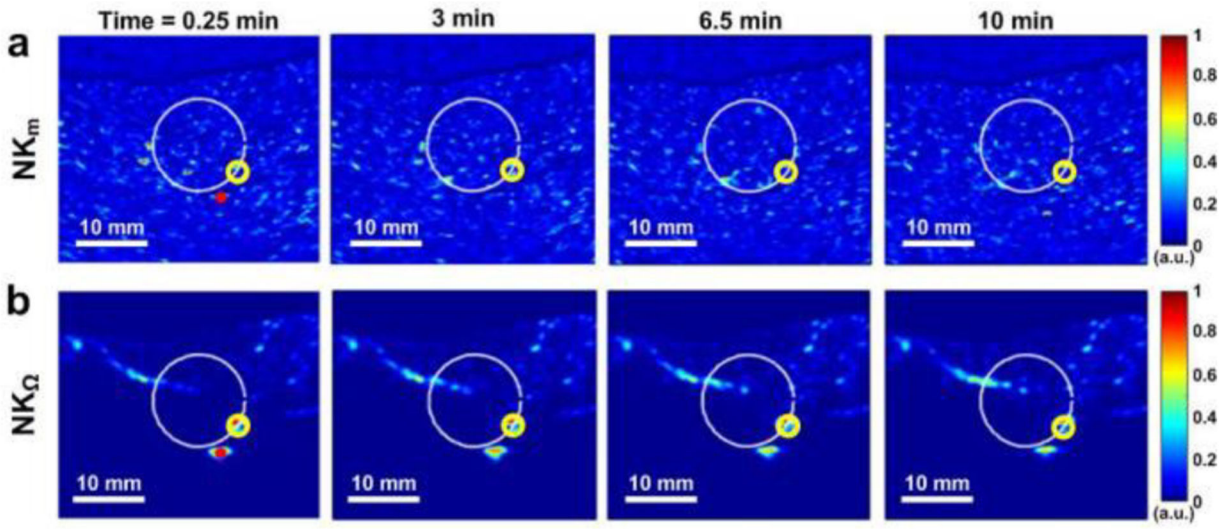

Figure 4.

(Color online) The corresponding normalized Nakagami parametric images of (a) shape (NK_m) and (b) scale (NK_Ω) parameters corresponding to the same example in Fig. 3.

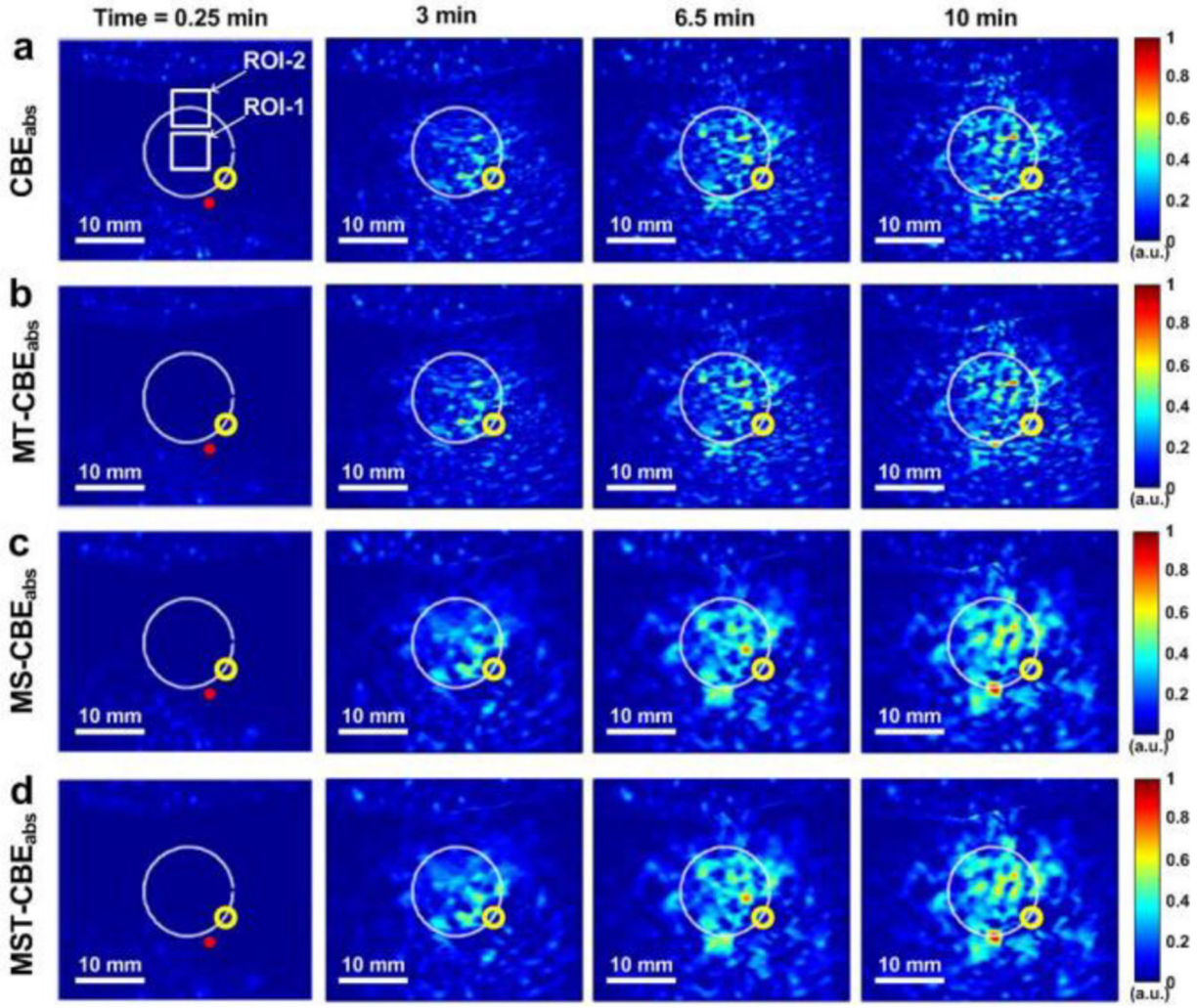

Figure 5.

(Color online) The corresponding normalized CBE maps of absolute component (CBE_{abs}) of the same example in Fig. 3 using four CBE_{abs} methods, including conventional CBE_{abs}, multi-temporal compounding CBE_{abs} (MT-CBE_{abs}), multi-spatial compounding CBE_{abs} (MS-CBE_{abs}), and MST-CBE_{abs}.

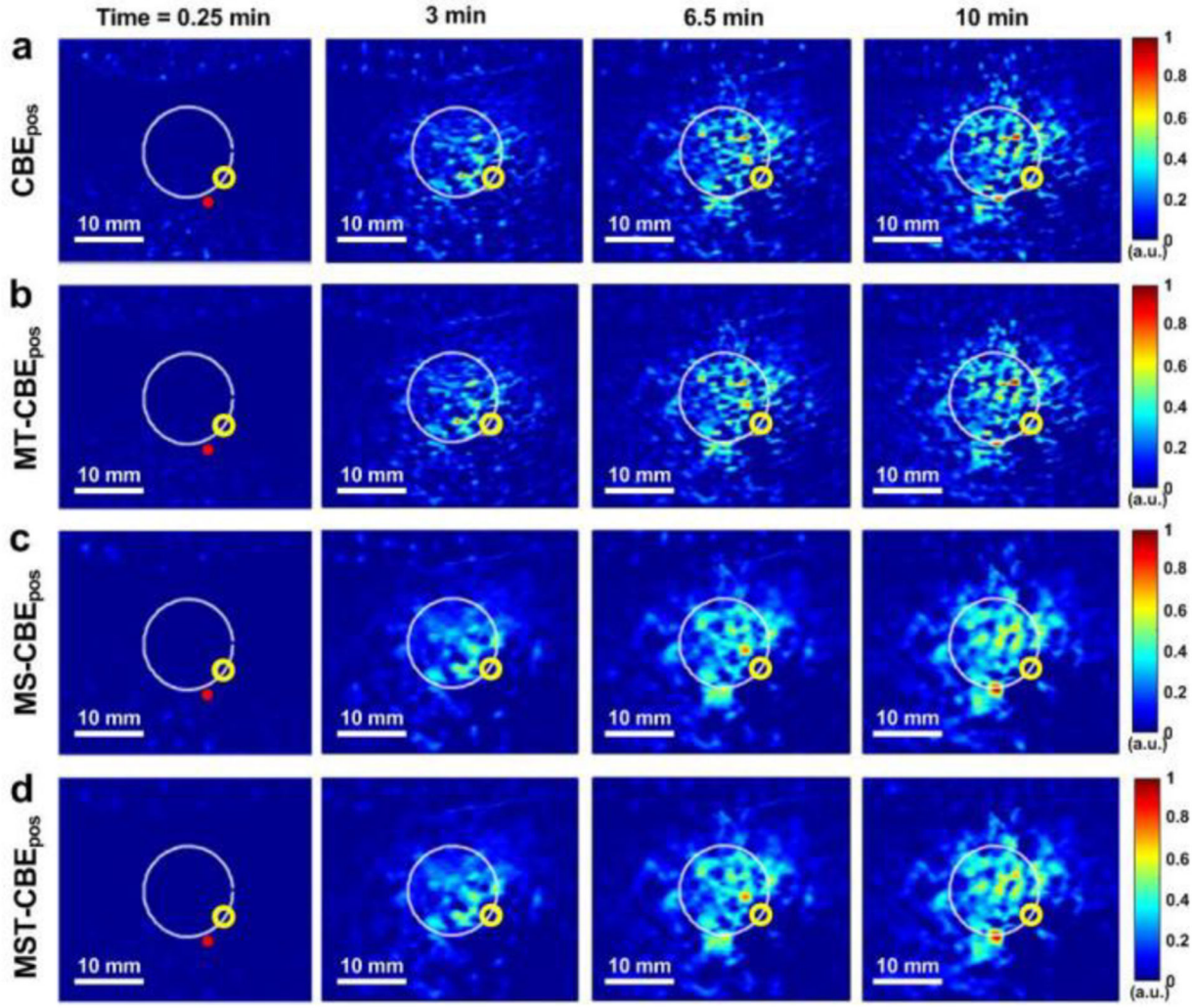

Figure 6.

(Color online) The corresponding normalized CBE maps of positive component (CBE_{pos}) of the same example in Fig. 3 using four CBE_{pos} methods, including conventional CBE_{pos}, MT-CBE_{pos}, MS-CBE_{pos}, and MST-CBE_{pos}.

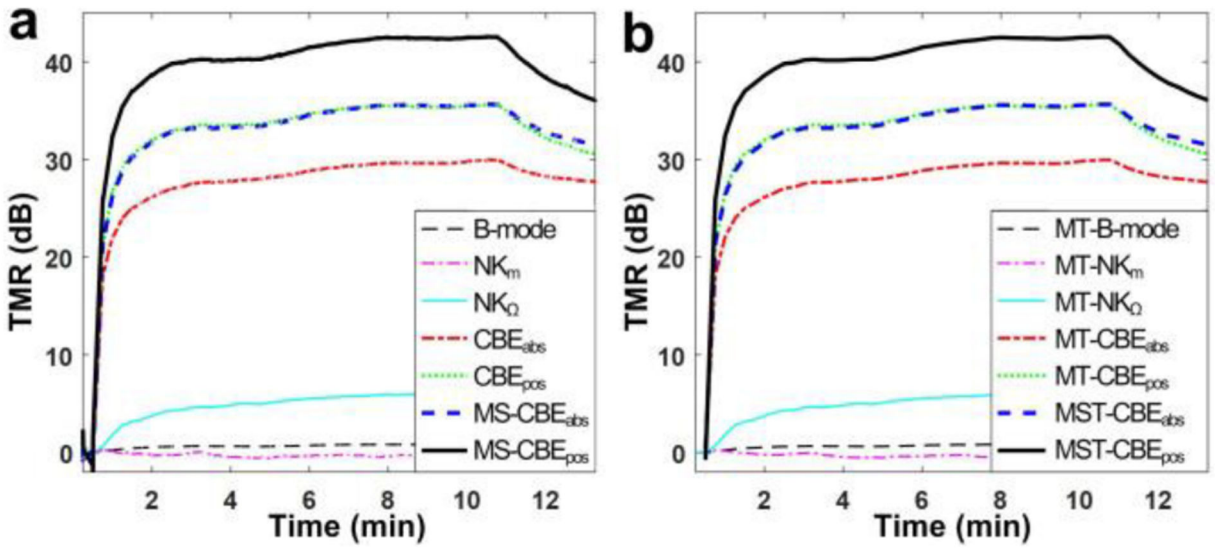

Figure 7.

(Color online) Examples of mean tissue modification ratio (TMR) curves over treatment duration of (a) seven monitoring methods of B-mode, NK_m, NK_Ω, CBE_{abs}, CBE_{pos}, MS-CBE_{abs}, and MS-CBE_{pos} and (b) the same methods combined with the MT estimation strategy.

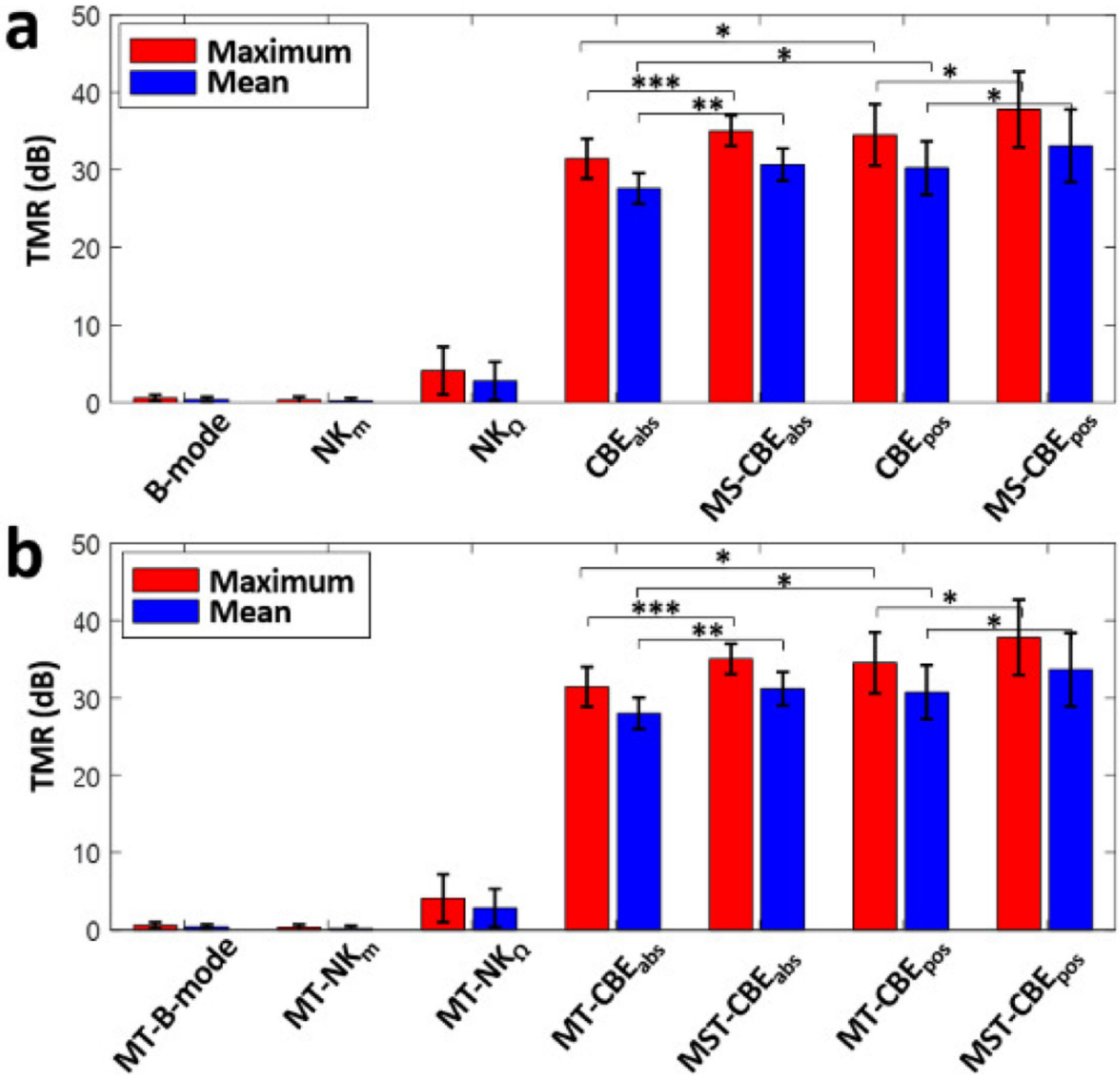

Figure 8.

(Color online) Statistical analysis of mean and maximum values of TMR curves of (a) seven monitoring methods (a) without and (b) with MT estimation strategy. *: $p < 0.05$, **: $p < 0.01$, and ***: $p < 0.005$, respectively.

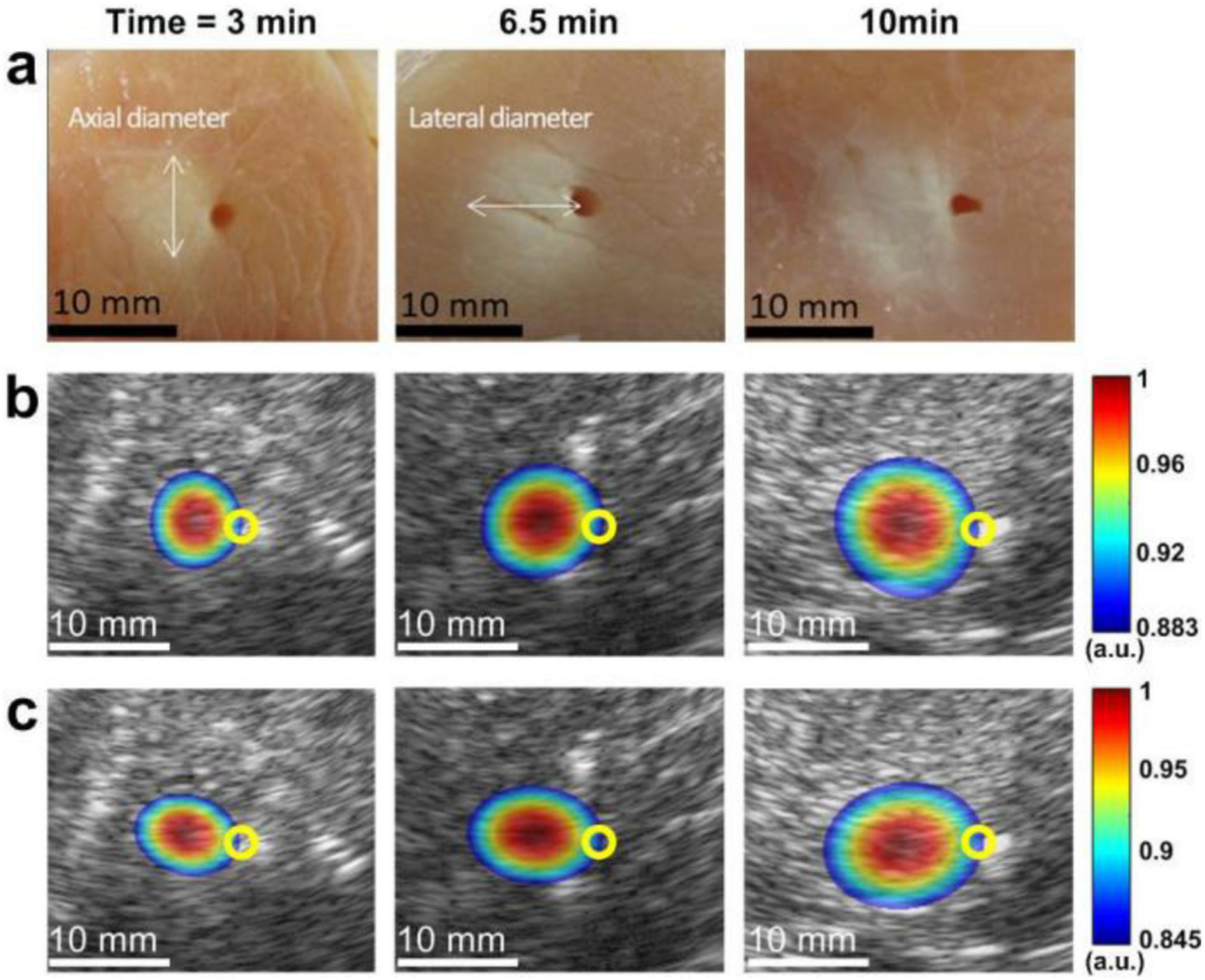

Figure 9.

(Color online) Examples of ablation zones from three separate cases (a) as in tissue sections, (b) estimated from fitted MST-CBE$_{abs}$ and (c) MST-CBE$_{pos}$ images at the treatment duration of 3, 6.5, and 10 min using the 180°-CBUS applicator, respectively. Thresholds of 0.883 and 0.845 were used in fitted MST-CBE$_{abs}$ and MST-CBE$_{pos}$, respectively, to define coagulation zones and are depicted as translucent contoured regions.

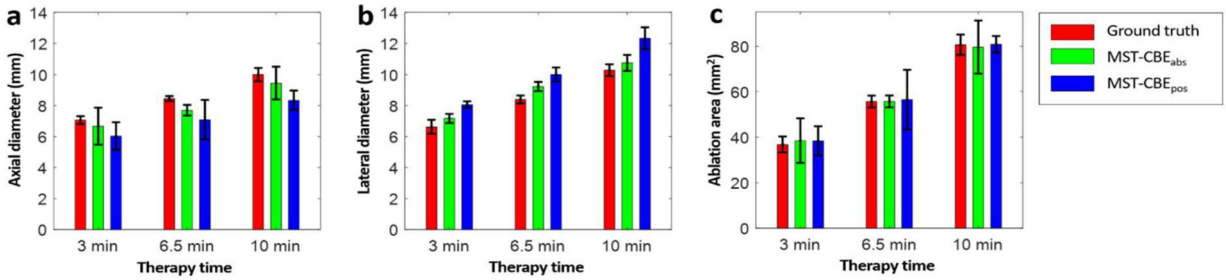

Figure 10.

(Color online) (a) Transverse and (b) radial lesion dimensions, and (c) areas within ablation zones of all samples assessed using tissue cross-section, MST-CBE_{abs}, and MST-CBE_{pos}, respectively.

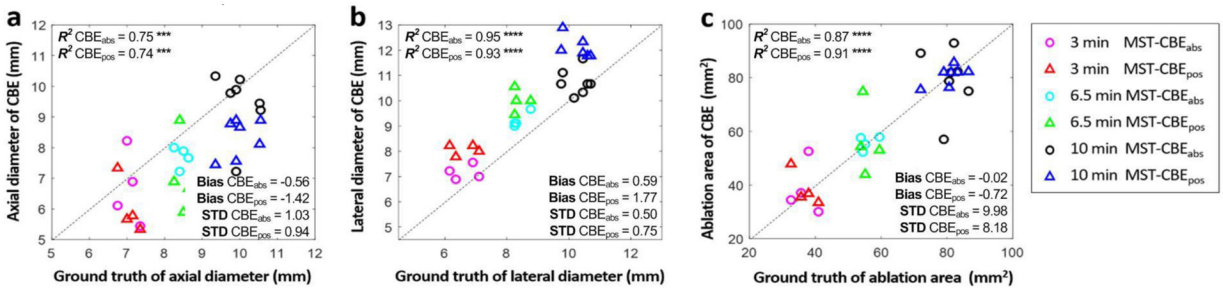

Figure 11.

(Color online) Agreement and Bland-Altman analyses of (a) all transverse and (b) radial lesion dimensions, and (c) areas within all ablation zones between the measured and estimated results. ***: $p < 0.005$ and ****: $p < 0.001$.

Table 1

Comparison of maximum TMR values between MST-CBE and other techniques.

Row - Column	B-mode	NK_m	NK_Ω	CBE_{abs}	CBE_{pos}
MST-CBE	37.21 ± 4.65 ****	37.45 ± 5.23 ****	33.71 ± 4.02 ****	6.37 ± 4.02 *	3.28 ± 2.28 *

*: $p < 0.05$ and

****: $p < 0.0001$

Table 2

Comparison of mean TMR values of CBE techniques with and without MS, MT, and MST estimation strategies.

Row - Column	MS-CBE_{abs}	MS-CBE_{pos}	MT-CBE_{abs}	MT-CBE_{pos}
CBE_{pos}	$-3.09 \pm 1.31^{**}$	/	$-0.39 \pm 0.05^{****}$	/
CBE_{pos}	/	$-2.88 \pm 2.12^{*}$	/	$-0.46 \pm 0.07^{****}$
MST-CBE_{abs}	$0.45 \pm 0.08^{****}$	/	$3.16 \pm 1.34^{**}$	/
MST-CBE_{pos}	/	$0.53 \pm 0.09^{****}$	/	$2.94 \pm 2.14^{*}$

*: $p < 0.05$,

**: $p < 0.01$, and

****: $p < 0.0001$